

Banner appropriate to article type will appear here in typeset article

# 1 DNS study of turbulent pipe flow with imposed 2 radial rotation

3 Alessandro Ceci<sup>1</sup>† and Sergio Pirozzoli<sup>1</sup>

4 <sup>1</sup>Dipartimento di Ingegneria Meccanica ed Aerospaziale, Sapienza University of Rome, Via Eudossiana  
5 18, 00184 Rome, Italy

6 (Received xx; revised xx; accepted xx)

7 We carry out direct numerical simulations (DNS) of fully developed turbulent pipe flow  
8 subjected to radial system rotation, examining a broad range of rotational speed and Reynolds  
9 number. In response to the imposed system rotation, strong secondary motions arise in the  
10 form of streamwise-aligned counter-rotating eddies, which engage significantly with the  
11 boundary layer, exerting a notable influence on the turbulent flow. At sufficiently high rotation  
12 numbers, a Taylor-Proudman region appears, marked by a constant mean axial velocity along  
13 the rotation axis. As rotation increases, local flow relaminarisation takes place starting at the  
14 suction side of the pipe, ultimately resulting in full relaminarisation when the rotation number  
15 is high enough. In this regime the near-wall region of the flow exhibits the typical hallmark  
16 of laminar Ekman layers, whose strength varies with the azimuthal position along the pipe  
17 perimeter. A predictive analytical formula for frictional drag is derived for the ultimate high-  
18 rotation regime which we blend with the classical formulas for non-rotating pipes, to obtain  
19 a full parametrisation of friction with respect to rotation and Reynolds number variations.

20 **Key words:** Pipe flow; Turbulence simulation; Rotating flows

---

## 21 1. Introduction

22 Flows in rotating passages are prevalent in technological applications, especially in turbo-  
23 machinery (Greitzer *et al.* 2007). In pipe flow, two canonical cases can be identified, in  
24 which the rotation axis is either parallel or orthogonal to the pipe axis. In the latter case  
25 on which we focus in the present work, Coriolis forces act on the fluid as body forces,  
26 breaking the azimuthal symmetry of the flow and inducing large-scale secondary motions  
27 in the cross-stream plane. In particular, turbulence is suppressed at the suction side of the  
28 duct, and enhanced at the pressure side, as highlighted in research dealing with rotating  
29 channels (Kristoffersen & Andersson 1993). In a pioneering work, Barua (1954) studied  
30 analytically laminar pipe flows with imposed radial rotation, obtaining estimates for the  
31 friction coefficient. However, no such theory exists for the case where the baseline pipe flow  
32 is turbulent, which makes it a compelling research case. Benton & Boyer (1966) studied the  
33 flow through rapidly rotating channels of various cross-section, from the experimental and

† Email address for correspondence: alessandro.ceci@uniroma1.it

34 analytical standpoint. For very high rotation rates, they showed that the significance of viscous  
 35 effects is confined to thin boundary layers along the channel walls. Solutions for both the  
 36 geostrophic region and the boundary layers were derived and integrated to yield the entire  
 37 velocity field. Experimental findings for a circular conduit were provided, demonstrating  
 38 favorable consistency with the theoretical framework.

39 Ito & Nanbu (1971) investigated experimentally the friction factor for fully developed  
 40 smooth pipe flow radially rotating at a constant angular velocity for bulk Reynolds numbers  
 41 in the range from 20 to 60000, presented empirical predictions for the friction factor in both  
 42 laminar and turbulent flow. Johnston *et al.* (1972) conducted experimental investigations  
 43 on fully developed turbulent channel flow under steady rotation about a spanwise axis.  
 44 They found that the Coriolis force components in the region of two-dimensional mean flow  
 45 impacted both local and global stability.

46 Kristoffersen & Andersson (1993) conducted direct numerical simulation (DNS) of fully  
 47 developed pressure-driven turbulent flow in a rotating channel at a fixed low Reynolds  
 48 number, for various rotational speeds. At the lowest rotational speed, turbulence statistics  
 49 were found to be barely affected, with opposite effects observed along the stable suction  
 50 side and the unstable pressure side. Turbulent Reynolds stresses were found to decrease near  
 51 the suction side at increasing rotational speed, whereas turbulence intensities increased on  
 52 the pressure side, with streamwise intensity and the Reynolds shear stress also increasing  
 53 at moderate rotational speed but suppressed at higher speed. The mean velocity profile was  
 54 found to become increasingly asymmetric at high rotational speeds, reflecting experimental  
 55 observations. Large-scale coherent structures were deemed to be responsible for transporting  
 56 highly turbulent fluid from the pressure side to the channel middle, enhancing the turbulence  
 57 levels. However, those structures were unstable for most rotation cases considered. Using  
 58 similarity arguments and leveraging experimental and numerical data, Ishigaki (1996)  
 59 demonstrated quantitative analogy between fully developed turbulent flows in curved pipes  
 60 and orthogonally rotating pipes.

61 Large-eddy simulations (LES) of turbulent flow in a rotating square duct at fixed low  
 62 Reynolds number were carried out by Pallares & Davidson (2000). Notable changes from  
 63 the non-rotating state were observed even at low rotation rates, driven by the secondary  
 64 motions near the duct corners. The Coriolis effect was found to generate a descending cross-  
 65 stream current in the duct core, enhancing streamwise vorticity and secondary motions that  
 66 convect upwards near the side walls and towards the duct centre. Rotation was found to  
 67 intensify turbulence near walls where the main shear vorticity aligns with the background  
 68 vorticity, and to reduce turbulence at the other walls. At the highest rotation rate considered  
 69 by those authors, the turbulence levels were found to decrease at the stable side due to flow  
 70 stabilisation into a Taylor–Proudman regime resulting from intensified Coriolis-induced  
 71 vertical convective transport of streamwise momentum. In a follow-up study, Pallares *et al.*  
 72 (2005) derived a predictive formula for the velocities and friction coefficients in a rotating  
 73 square duct based on the solution of the simplified set of momentum equations. At rotational  
 74 speed, the Ekman layers were found to be responsible for large share of the pressure drop.

75 Experimental investigations of rapidly-rotating turbulent square and rectangular duct  
 76 flows were conducted by Mårtensson *et al.* (2002), at low-to-moderate Reynolds number.  
 77 Examination of inclined duct flow confirmed the significance of the normal component of  
 78 the rotation vector in understanding rotational effects. Analysis of various duct geometries  
 79 indicated that the contribution to pressure drop from near-wall Ekman layers dominated,  
 80 yielding an increase of the friction coefficient with the rotational speed. Further turbulent  
 81 channel flow DNS under rotation have been carried-out by Rotation effects were also studied  
 82 by Dai *et al.* (2015); Fang *et al.* (2017) for square ducts and by Rosas *et al.* (2021) for  
 83 elliptical pipes. At moderate rotation rate, the suction side was found to relaminarise first as

84 Coriolis forces dominate the energy transfer mechanisms, and a Taylor-Proudman region was  
 85 observed at high rotation numbers. DNS of radially rotating turbulent pipe flow by Zhang &  
 86 Wang (2019) revealed asymmetric flow patterns, with high-speed flow on the pressure side of  
 87 the pipe and low-speed flow on the suction side, driven by Coriolis forces. Secondary motions  
 88 were observed to emerge, which eventually disappear at high enough rotational speed. Those  
 89 authors also found that the Coriolis force affected the budget of Reynolds shear stress, leading  
 90 to asymmetrical profiles and decrease of Reynolds stresses at increasing rotational speed.

91 The key controlling parameter in rotating duct flow is the rotation number, defined as  
 92 the ratio of a typical rotation velocity (e.g. angular velocity by hydraulic diameter) to the  
 93 flow bulk velocity. Typical rotation numbers in turbomachinery applications are in the range  
 94 0.3–0.38, as documented in the studies of Coletti *et al.* (2012) and Coletti *et al.* (2014). Higher  
 95 rotation rates are nevertheless significant in various engineering applications, particularly  
 96 in gas turbine engines, for which rotation number can be as high as 3.33 – 10 (Atkins  
 97 & Kanjirakkad 2014; Jackson *et al.* 2021; Luberti *et al.* 2021; Sun *et al.* 2022; Visscher  
 98 *et al.* 2011). Furthermore, experimental studies of cooling systems such as Morris (1996),  
 99 emphasise the relevance of rotation numbers of about two in typical engine conditions,  
 100 at which the cooling performance is severely affected from secondary flows generated by  
 101 Coriolis forces. Liou *et al.* (2007) numerically simulated duct flow with rotation number  
 102 in the range between zero to two, and asserted that there is a strategic need to extend the  
 103 experimental data to emulate more closely realistic engine conditions by extending Reynolds  
 104 number and rotation number simultaneously. This shortcoming is also well portrayed in the  
 105 study of Ligrani (2013).

106 Given this background, it is clear that there is a large demand for improving the  
 107 knowledge of flows in ducts in the presence of rotation, since: 1) existing DNS and LES are  
 108 restricted to low Reynolds number, at which turbulence is barely developed; 2) experimental  
 109 measurements are scarce, and by the way affected by substantial uncertainties; 3) there is  
 110 a lack of data for the technologically outstanding case of flow in a rotating circular pipe;  
 111 4) predictive friction formulas for duct flow with are not sufficiently qualified, and mainly  
 112 based on empirical fitting of existing (sparse) data. The goal of this work is then to fill in the  
 113 existing gap of knowledge, and for that purpose we carry out DNS of flow in a smooth circular  
 114 pipe subjected to radial rotation, at sufficiently high Reynolds number to be representative of  
 115 realistic flow instances, and in a wide range of rotation numbers. The paper is organised as  
 116 follows. In §2 we present the DNS dataset used for the analysis. The flow structure and the  
 117 turbulence statistics are presented in §3, and friction is analysed in detail in §4. Concluding  
 118 comments are made in §5.

## 119 2. The numerical dataset

120 The DNS solver relies on a second-order finite-difference discretisation of the incompressible  
 121 Navier–Stokes equations in cylindrical coordinates, utilizing the marker-and-cell method to  
 122 maintain discrete conservation of the total kinetic energy (Orlandi 2000). To ensure a constant  
 123 mass flow rate, uniform volumetric forcing is applied to the axial momentum equation. The  
 124 Poisson equation resulting from enforcement of the divergence-free condition is efficiently  
 125 solved through double trigonometric expansion in periodic axial and azimuthal directions,  
 126 coupled with tridiagonal matrix inversion in the radial direction (Kim & Moin 1985). The  
 127 polar singularity at the pipe axis is handled as suggested by Verzicco & Orlandi (1996). Time  
 128 advancement relies on a hybrid third-order low-storage Runge–Kutta algorithm, whereby  
 129 diffusive terms are treated implicitly and convective terms are treated explicitly. Implicit  
 130 treatment of the convective terms in the azimuthal direction is also used to mitigate the time  
 131 step restriction (Akselvoll & Moin 1996; Wu & Moin 2008). The code is optimised for GPU

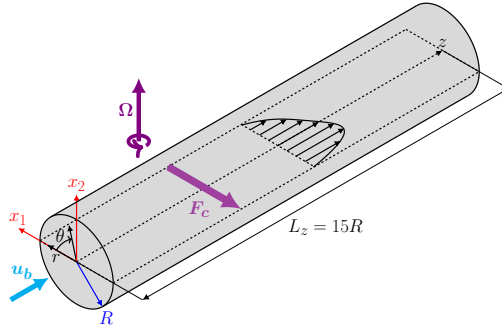


Figure 1: Definition of coordinate system for DNS of rotating pipe flow.  $z, r, \theta$  are the axial, radial and azimuthal coordinates, respectively.  $R$  is the pipe radius,  $L_z$  the pipe length, and  $u_b$  is the bulk velocity.  $\Omega$  is the angular velocity, and  $\mathbf{F}_c$  is the resultant mean Coriolis force. [The Cartesian coordinates  \$x\_1, x\_2\$  define positions in the cross-stream plane.](#)

132 clusters using CUDA Fortran and OpenACC directives, with CUFFT libraries facilitating  
133 fast Fourier transforms (FFTs) (Fatica & Ruetsch 2014).

134 A sketch of the computational domain is shown in figure 1. The radial coordinate measured  
135 from the pipe axis is denoted as  $r$ . Numerical simulations are carried out using periodic  
136 boundary conditions in the axial ( $z$ ) and azimuthal ( $\theta$ ) directions. The effect of rotation is  
137 accounted for by augmenting the Navier-Stokes equations with the Coriolis forces,

$$138 \quad \mathbf{F}_c = 2\Omega \begin{bmatrix} -u_z \sin \theta \\ u_z \cos \theta \\ u_\theta \cos \theta - u_r \sin \theta \end{bmatrix}, \quad (2.1)$$

139 where the angular velocity ( $\Omega$ ) is assumed to be parallel to the polar ( $x_2$ ) axis. The wall  
140 distance is hereafter denoted as  $y$ . As noted in previous studies, centrifugal forces are not  
141 explicitly added as they are absorbed into the pressure term (Kristoffersen & Andersson  
142 1993). As illustrated in figure 1, the primary effect of rotation normal to the pipe axis is the  
143 onset of Coriolis forces which in average act orthogonal to both the pipe axis and the rotation  
144 axis, resulting in increased shear at the pressure side of the pipe, and shear suppression at the  
145 suction side. The flow is controlled by two parameters, namely the bulk Reynolds number,  
146  $Re_b = 2Ru_b/\nu$ , and the rotation number,  $N = \Omega R/u_b$ , with  $R$  the pipe radius,  $u_b$  the bulk  
147 velocity and  $\nu$  the fluid kinematic viscosity. [This definition is used here as it emphasises the maximum peripheral velocity with respect to the bulk velocity, but one should be careful and note that several previous studies of rotating ducts rather define the rotation number based on the hydraulic diameter, here the pipe diameter.](#) The friction Reynolds number  $Re_\tau$  is  
148 also an important flow parameter, defined as  $Re_\tau = Ru_\tau^*/\nu$ , with  $u_\tau^* = (\tau_w^*/\rho)^{1/2}$  the global  
149 friction velocity and  $\tau_w^*$  the azimuthally averaged mean wall shear stress. The flow properties  
150 normalised by these global viscous scales are hereafter denoted with an asterisk. In all DNS  
151 the pipe length is taken to be  $L_z = 15R$ , which we have found to be sufficient to achieve  
152 convergence of all the statistics herein reported, [as shown in the paper appendix](#). The grid  
153 points are clustered towards the pipe walls according to the stretching function developed  
154 by Pirozzoli & Orlandi (2021), whereas the grid points are uniformly spaced in the  $z$  and  
155  $\theta$  directions. [Adequacy of the grid resolution has been evaluated through a grid sensitivity](#)  
156 [analysis, also reported in the appendix.](#)

157 A complete list of the simulations that we have carried out is given in table 1. A one-  
158 decade range of Reynolds numbers has been explored, along with a wide range of rotation  
159 numbers, including cases with weak rotation as well as cases in which rotation dominates.  
160

$Re_b$	$Re_\tau$	$N$	$N_\tau$	$N_z \times N_r \times N_\theta$	$\lambda \times 10^{-2}$	Line
17000	509	0.0078125	0.130	769 $\times$ 97 $\times$ 769	2.865	-
17000	516	0.015625	0.257	769 $\times$ 97 $\times$ 769	2.944	-
17000	523	0.03125	0.507	769 $\times$ 97 $\times$ 769	3.032	—
17000	539	0.0625	0.986	769 $\times$ 97 $\times$ 769	3.211	—
17000	566	0.125	1.87	769 $\times$ 97 $\times$ 769	3.557	—
17000	610	0.25	3.48	769 $\times$ 97 $\times$ 769	4.121	—
17000	669	0.5	6.34	769 $\times$ 97 $\times$ 769	4.963	—
17000	856	2.0	19.8	769 $\times$ 97 $\times$ 769	8.117	—
17000	1004	4.0	33.8	769 $\times$ 97 $\times$ 769	11.17	—
17000	1187	8.0	57.2	769 $\times$ 97 $\times$ 769	15.62	—
44000	1188	0.01	0.185	1793 $\times$ 165 $\times$ 1793	2.334	-
44000	1296	0.1	1.69	1793 $\times$ 165 $\times$ 1793	2.777	-
44000	1405	0.5	7.83	1793 $\times$ 165 $\times$ 1793	3.262	-
44000	1761	2.0	25.0	1793 $\times$ 165 $\times$ 1793	5.123	-
44000	2043	4.0	43.0	1793 $\times$ 165 $\times$ 1793	6.902	-
44000	2418	8.0	72.7	1793 $\times$ 165 $\times$ 1793	9.670	-
82500	2077	0.01	0.198	3073 $\times$ 244 $\times$ 3073	2.027	-
82500	2294	0.1	1.79	3073 $\times$ 244 $\times$ 3073	2.474	-
82500	2379	0.5	8.66	3073 $\times$ 244 $\times$ 3073	2.662	-
82500	2833	2.0	29.1	3073 $\times$ 244 $\times$ 3073	3.773	-
82500	4595	16.0	143	3073 $\times$ 244 $\times$ 3073	9.930	-
133000	3181	0.01	0.209	4609 $\times$ 328 $\times$ 4609	1.830	-
133000	3527	0.1	1.88	4609 $\times$ 328 $\times$ 4609	2.250	—
133000	3663	0.5	9.15	4609 $\times$ 328 $\times$ 4609	2.387	—
133000	4110	2.0	32.3	4609 $\times$ 328 $\times$ 4609	3.056	—
133000	6573	16.0	161	4609 $\times$ 328 $\times$ 4609	7.817	—

Table 1: Flow parameters for DNS of rotating pipe flow. The bulk Reynolds number defined as  $Re_b = 2Ru_b/\nu$ , with  $R$  the pipe radius,  $u_b$  the bulk velocity and  $\nu$  the fluid kinematic viscosity.  $N = \Omega R/u_b$  is the rotation number and  $N_\tau = \Omega R/u_\tau^*$  is the friction rotation number with the global friction velocity.  $N_z, N_r, N_\theta$  are respectively the number of grid points in the axial, radial and azimuthal direction. The global friction factor is  $\lambda = 8\tau_w^*/\rho u_b^2$ , with  $\tau_w^*$  the azimuthally averaged mean wall shear stress and  $\rho$  the fluid density.  $Re_\tau = Ru_\tau^*/\nu$  is the friction Reynolds number, with  $u_\tau^* = (\tau_w^*/\rho)^{1/2}$  the mean friction velocity.

163 For the sake of clarity, capital letters will be used to denote flow properties averaged along the  
 164 axial direction and in time, and fluctuations thereof will be denoted with lowercase letters.  
 165 Instantaneous properties will be denoted with tilde superscripts. Angular brackets will be  
 166 used to denote the averaging operator.

### 167 3. Flow organisation

168 As a first step, we analyze the flow organisation from representative instantaneous snapshots  
 169 at the two extreme Reynolds numbers, namely  $Re_b = 17000$  and  $Re_b = 133000$ . Specifically,  
 170 in figures 2-3 we show the contours of the axial velocity in the cross-stream plane, and  
 171 in figures 4-5 we show the axial velocity contours in a cylindrical shell at small distance  
 172 ( $y^* = 15$  for the non-rotating case) from the wall. The former are used to get insight into the  
 173 large-scale bulging motions which connect the near-wall region with the bulk flow, whereas

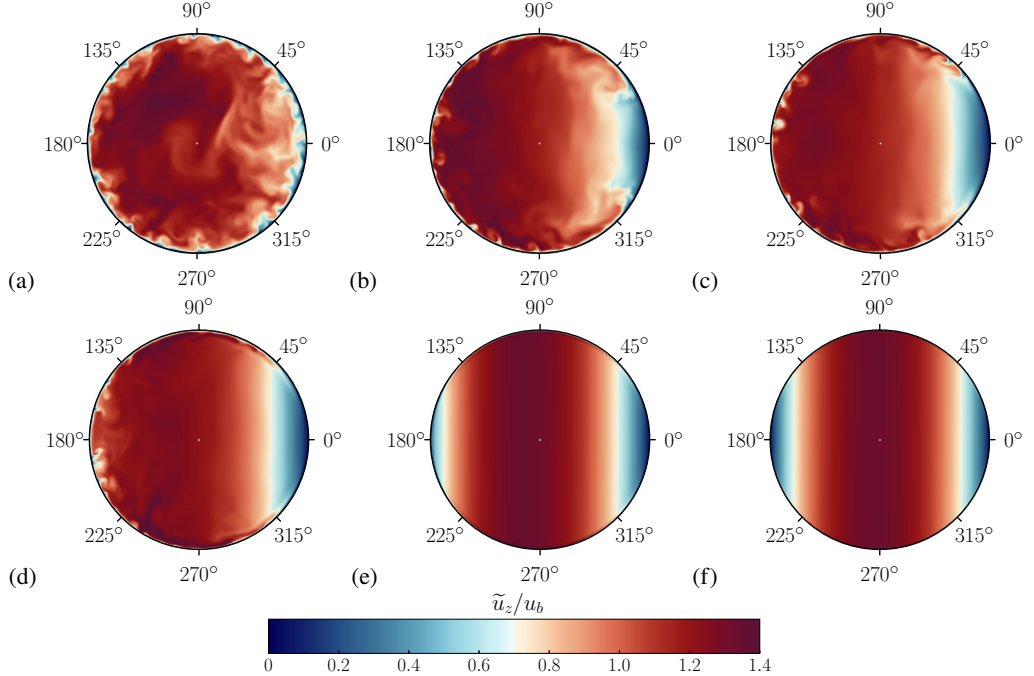


Figure 2: Instantaneous axial velocity contours at  $Re_b = 17000$  in the cross-stream plane. Contour levels ranging from 0 to 1.4 are shown, in colour scale from blue to red. The pressure side of the pipe is on the left, and the suction side is on the right of each sub-panel. Various rotation numbers are considered: (a)  $N = 0.0078125$ , (b)  $N = 0.125$ , (c)  $N = 0.25$ , (d)  $N = 0.5$ , (e)  $N = 2.0$ . (f)  $N = 8.0$ .

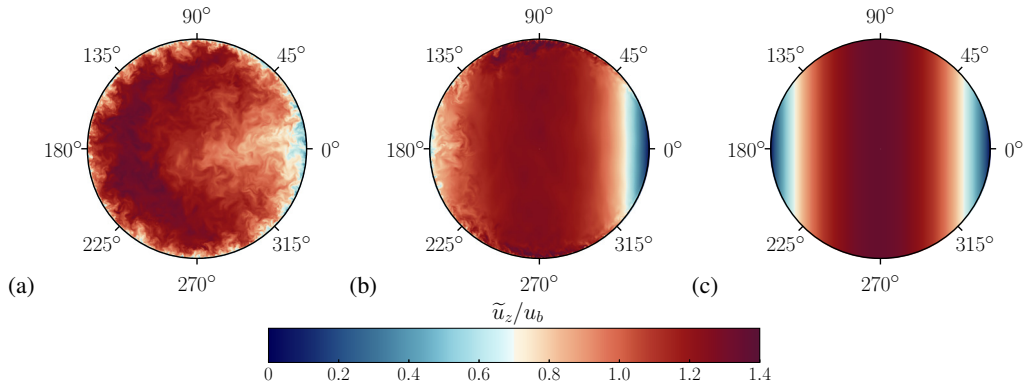


Figure 3: Instantaneous axial velocity contours at  $Re_b = 133000$  in the cross-stream plane. Contour levels ranging from 0 to 1.4 are shown, in colour scale from blue to red. The pressure side of the pipe is on the left, and the suction side is on the right of each sub-panel. Various rotation numbers are considered: (a)  $N = 0.01$ , (b)  $N = 0.5$ , (c)  $N = 16.0$ .

174 the latter are used to get insight into the modifications of the near-wall streaks resulting from  
 175 pipe rotation. For the sake of correct interpretation of the figures we note that the azimuthal  
 176 angle  $\theta$  as defined in figure 1 is such that  $\theta = 0^\circ \pm 15^\circ$  corresponds to the suction side of the  
 177 pipe, whereas  $\theta = 180^\circ \pm 15^\circ$  corresponds to pressure side. Coriolis forces are such that in

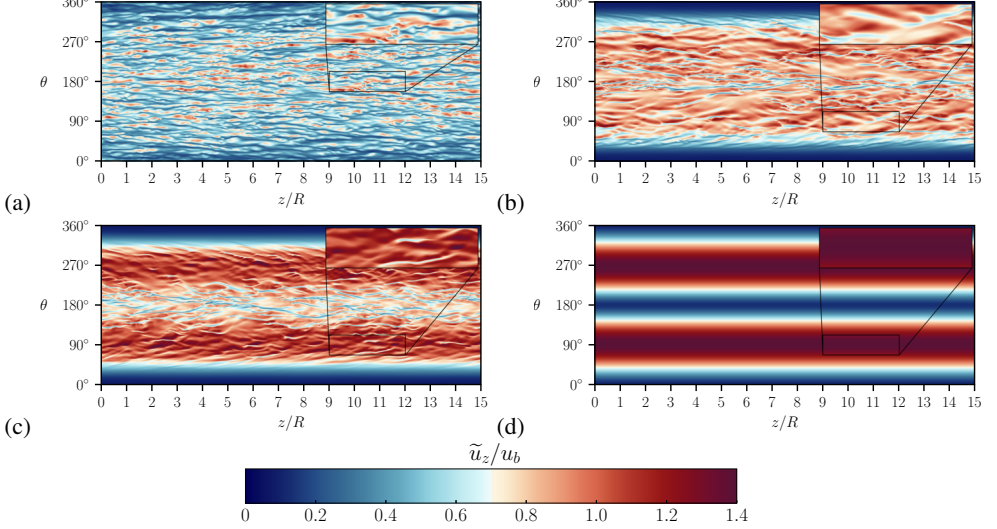


Figure 4: Instantaneous axial velocity contours at  $Re_b = 17000$  in an unrolled cylindrical shell at a distance  $y^* = 15$  from the wall (evaluated in the non-rotating case). Contour levels ranging from 0 to 1.4 are shown, in colour scale from blue to red. The insets in the top-right corner of each panel report magnified views of a small portion of the shell. Various rotation numbers are considered: (a)  $N = 0.0078125$ , (b)  $N = 0.25$ , (c)  $N = 0.5$ , (d)  $N = 8.0$ .

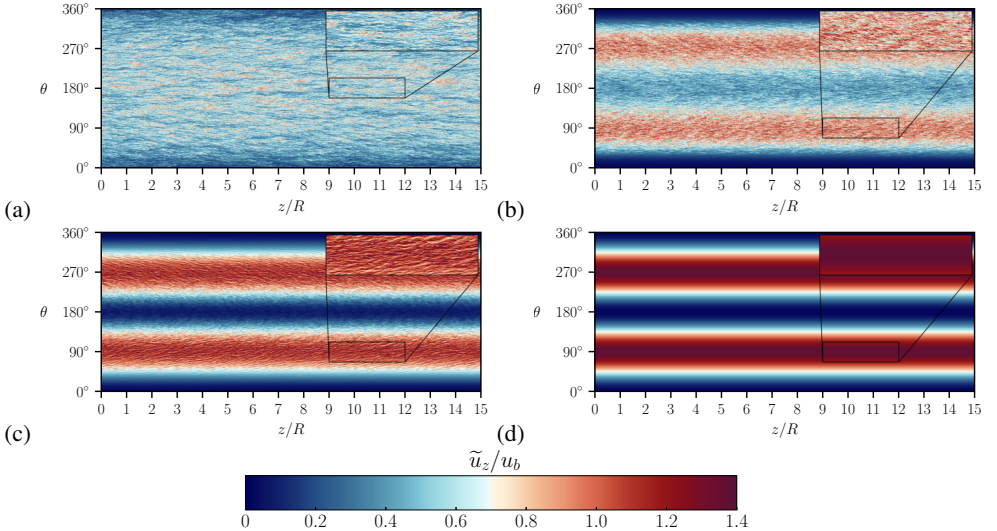


Figure 5: Instantaneous axial velocity ( $u_z/u_b$ ) at  $Re_b = 133000$  in an unrolled cylindrical shell at a distance  $y^* = 15$  from the wall (evaluated in the non-rotating case). Contour levels ranging from 0 to 1.4 are shown, in colour scale from blue to red. The insets in the top-right corner of each panel report magnified views of a small portion of the shell. Various rotation numbers are considered: (a)  $N = 0.01$ , (b)  $N = 0.5$ , (c)  $N = 2.0$ , (d)  $N = 16.0$ .

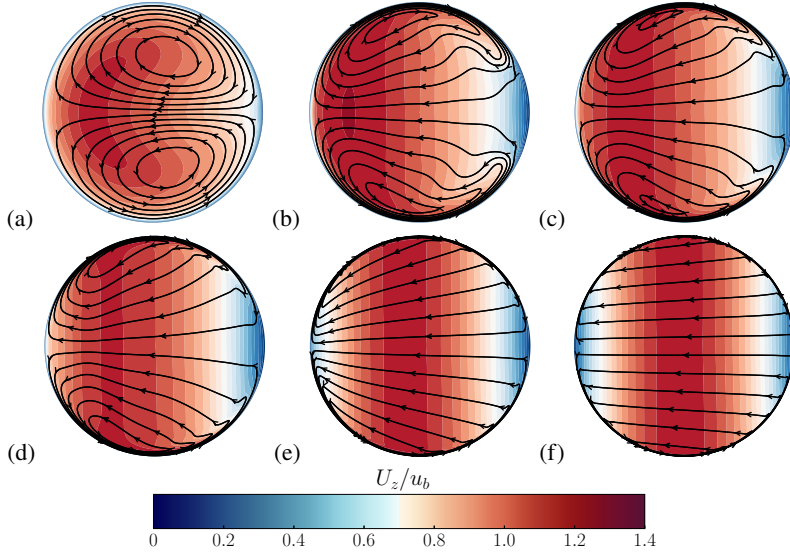


Figure 6: Mean axial velocity contours with superposed cross-flow streamlines, at  $Re_b = 17000$ . Twenty-four contour levels ranging from 0 to 1.4 are shown, in colour scale from blue to red. The pressure side of the pipe is on the left, and the suction side is on the right of each sub-panel. Various rotation numbers are considered: (a)  $N = 0.0078125$ , (b)  $N = 0.125$ , (c)  $N = 0.25$ , (d)  $N = 0.5$ , (e)  $N = 2.0$ , (f)  $N = 8.0$ .

average momentum is transported from the suction side towards the pressure side (Zhang & Wang 2019). The angles  $\theta = 90^\circ, 270^\circ$  correspond to the north and south pole of the pipe, respectively, along which the effects of rotation is most active. The first important information gained from the visualisations is that, even at modest rotation number (less than about 0.01) the effect of rotation is quite apparent on the suction side, which shows a visible momentum defect with respect to the pressure side. Bulging motions are instead still observed on the rest of the pipe perimeter. As the rotation number increases, the zone with reduced momentum at the suction side of the pipe becomes progressively more extended, and severe reduction of the turbulence activity is visible at  $N \gtrsim 0.1$ . At higher rotation numbers suppression of turbulence is also visible within the pipe core, and hints of flow relaminarisation become visible also on the pressure side at  $N \gtrsim 1$ . Eventually, at high rotation rates, the flow tends to become symmetric about the polar axis, and the velocity field tends to become organised in bands parallel to it. The relaminarisation process is best observed in the near-wall shells. At low rotation numbers streaks dominate the near-wall region, although some evidence for their local suppression at  $\theta \approx 0^\circ$  are visible. At intermediate rotation numbers streaks become progressively confined about the poles of the pipe, and they tend to vanish on the pressure side as well. At high rotation numbers, the flow no longer shows any sign of turbulence activity.

Since the flow exhibits homogeneity in the axial direction, its statistical characteristics solely rely on the azimuthal and radial coordinates. The mean axial velocity within the cross-stream plane is depicted in figure 6 for flow cases with  $Re_b = 17000$ , at various rotation numbers. Representative cross-flow streamlines are superimposed to the velocity contours to emphasise the variations in secondary motions as the rotation number changes. At low-to-moderate  $N$  (panels (a)-(d)), a notable alteration involves the symmetry breaking with respect to the polar axis, which implies gradual increase of axial momentum on the pressure side of the pipe (left) and a decrease on the suction side (right), on account of Coriolis forces.

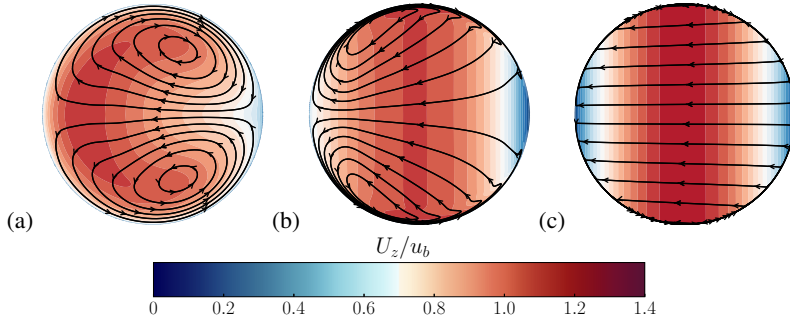


Figure 7: Mean axial velocity contours with superposed cross-flow streamlines, at  $Re_b = 133000$ . Twenty-four contour levels ranging from 0 to 1.4 are shown, in colour scale from blue to red. The pressure side of the pipe is on the left, and the suction side is on the right of each sub-panel. Various rotation numbers are considered: (a)  $N = 0.01$ , (b)  $N = 0.5$ , (c)  $N = 16.0$ .

Consequently, secondary motions emerge in the form of two counter-rotating eddies that facilitate momentum redistribution across the pipe cross-section, with primary flow moving from the suction to the pressure side along the horizontal symmetry axis and return motion occurring along the circumference of the pipe. Remarkably, at low  $N$ , these secondary motions closely resemble those predicted to form under laminar flow conditions (Barua 1954). As the rotation number increases, there is a discernible trend towards uniformity in mean velocity along the vertical direction, accompanied by a tendency for the momentum deficit at the suction to be compensated, resulting in symmetrisation of the flow field. This observed phenomenon distinctly marks the onset of Taylor-Proudman columns (Proudman 1916; Taylor 1917), characterised by tendency for the velocity to be constant along the axis of rotation, with no tilting or stretching of material lines parallel to this axis. At extreme rotation numbers, the secondary motions correspondingly take the form of right-to-left cross-stream motion, with return motions barely noticeable and confined to the near-wall proximity. Identical cross-stream flow information is presented in figure 7 for flow cases with  $Re_b = 133000$ . A remarkably similar flow pattern is discerned at corresponding values of the rotation number, for instance, comparing panels (a) and (d) of figure 6 with panels (a) and (b) of figure 7. This observation reinforces the idea that rotational effects on the mean flow properties are relatively unaffected by changes in the flow Reynolds number.

Due to the rearrangement of the flow, significant changes occur in wall friction as  $N$  varies. To examine this effect, figure 8 illustrates the local streamwise wall shear stress,  $\tau_w/\rho = \nu \partial U_z / \partial y|_w$ , normalised either by the reference dynamic pressure  $\rho u_b^2$  (left panels) or the mean wall shear stress  $\tau_w^*$  (right panels). A polar diagram is employed for clarity. The figure clearly demonstrates that even at very low rotational speeds, friction is nearly completely suppressed at the suction side of the pipe ( $\theta = 0$ ). Conversely, the behavior on the pressure side ( $\theta = \pi$ ) is non-monotonic, where the local streamwise wall shear stress initially increases due to local acceleration of the bulk flow, then abruptly declines beyond  $N \approx 1$ , signifying the dominance of rotation and the concentration of momentum around the vertical axis of the pipe. Friction at the poles of the pipe ( $\theta = 90^\circ, 270^\circ$ ) exhibits a monotonically increasing trend with the rotation number, on account of local thinning of the boundary layer, as detailed further ahead. At higher values of  $N$  considered, the local friction tends to attain a universal distribution when scaled by its mean value, regardless of the Reynolds number.

The mean axial velocity profiles are shown in outer scaling in figure 9. For the sake of clarity, the radial profiles are shown in the interval  $\theta = [0, 90^\circ]$  along the pipe perimeter. Due to flow symmetry, this interval is sufficient to fully describe the state of the axial velocity in

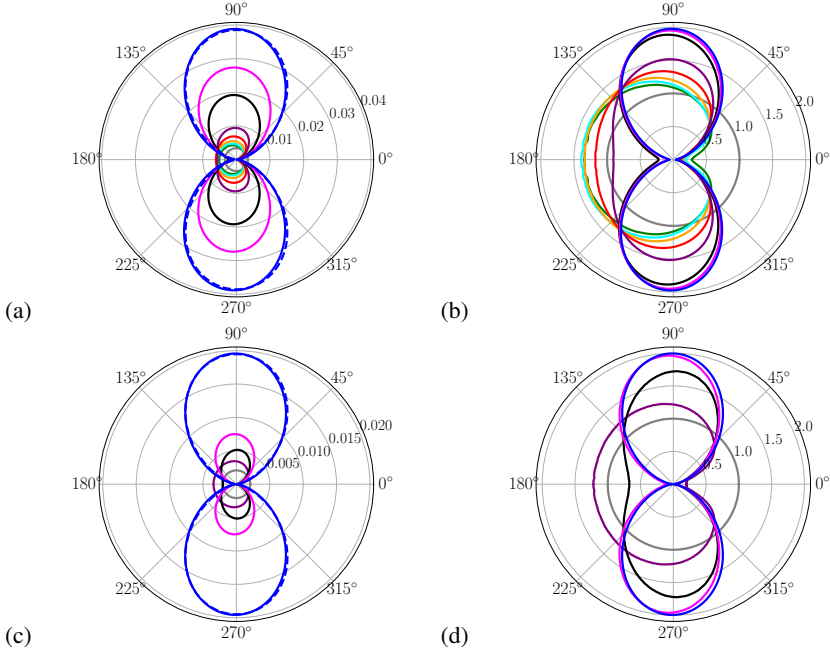


Figure 8: Polar distribution of the local streamwise wall shear stress ( $\tau_w$ ), normalised by either the reference dynamic pressure  $\rho u_b^2$  (a, c), or the mean wall shear stress  $\tau_w^*$  (b, d), at  $Re_b = 17000$  (a, b), and  $Re_b = 133000$  (c, d). The color codes correspond to different values of  $N$ , as given in table 1, gray denoting cases without rotation. The dashed blue line in panels (a, c) denotes the predictive formula given in equation (4.4).

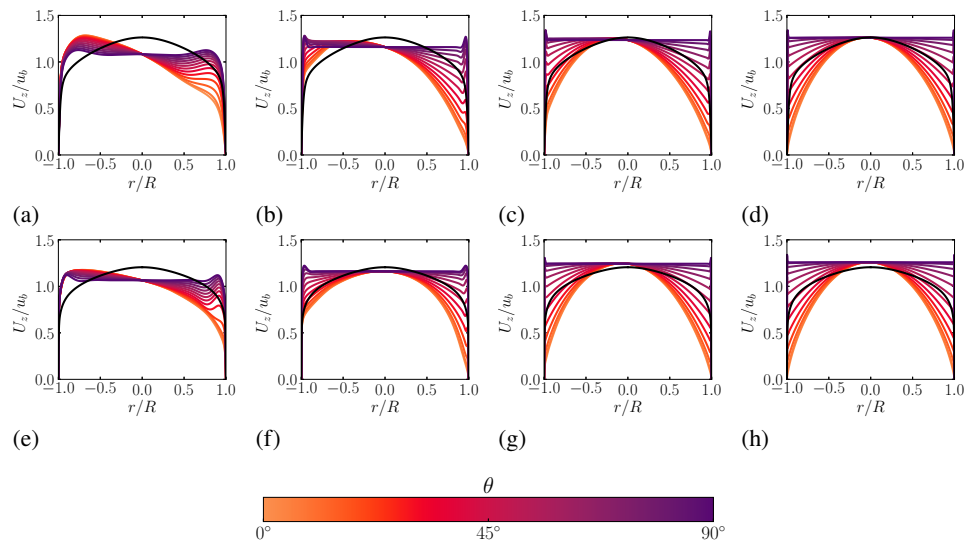


Figure 9: Radial profiles of outer-scaled axial velocity at various azimuthal positions, for flow cases at  $Re_b = 17000$  (a-d), and  $Re_b = 133000$  (e-h). Only the interval  $\theta = [0^\circ, 90^\circ]$  is shown, at stations spaced  $7.5^\circ$  apart, with negative values of  $r$  signifying profiles taken at  $\theta + 180^\circ$ . (a)  $N = 0.03125$ , (b)  $N = 0.5$ , (c)  $N = 2.0$ , (d)  $N = 8.0$ . (e)  $N = 0.1$ , (f)  $N = 0.5$ , (g)  $N = 2.0$ , (h)  $N = 16.0$ . The black solid line denotes the mean axial velocity profile in the non-rotating case.

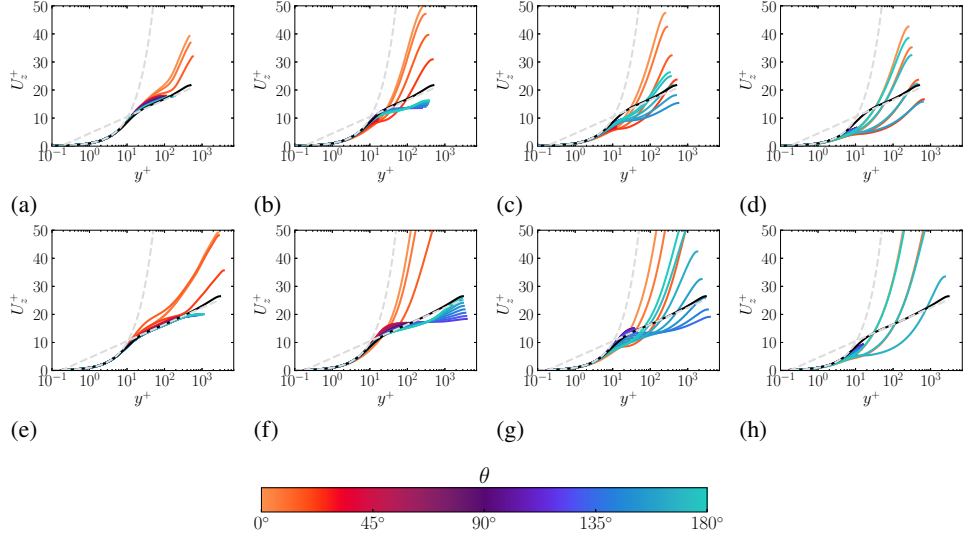


Figure 10: Wall-normal profiles of inner-scaled axial velocity, at various azimuthal positions spaced  $7.5^\circ$  apart, for flow cases at  $Re_b = 17000$  (a-d), and  $Re_b = 133000$  (e-h). Only the interval  $\theta = [0^\circ, 180^\circ]$  is shown. (a)  $N = 0.03125$ , (b)  $N = 0.5$ , (c)  $N = 2.0$ , (d)  $N = 8.0$ . (e)  $N = 0.1$ , (f)  $N = 0.5$ , (g)  $N = 2.0$ , (h)  $N = 16.0$ . The black solid line denotes the mean axial velocity profile in the non-rotating case. The dashed gray lines depict the compound law-of-the wall  $U^+ = y^+$ ,  $U^+ = \log y^+ / 0.387 + 4.53$ .

the pipe. The axial velocity for the non-rotating case ( $N = 0$ ) is also reported for reference, which is obviously symmetrical. As rotation sets in, the velocity profile along the horizontal symmetry axis (in orange shades) is immediately broken, and the peak value is shifted from the pipe centre to the pressure side of the pipe due to the presence of secondary motions in the cross-stream direction. The tendency of the axial velocity peak to shift towards the pressure side of the pipe, is, however, non-monotonic. As the rotation number approaches unity, in fact the peak value of the axial velocity moves back towards the centre of the pipe, as shown in panels (b) to (d) of figure 9, and the velocity profiles again become symmetric with respect to the origin. As for the velocity profiles along the polar direction (in purple shades), they show a sudden tendency to flatten out in the middle of the pipe, whereas peaks tend to arise towards the pipe walls, which are associated with the formation of Ekman layers due to rotation. This tendency is exacerbated at high  $N$ , at which the mean axial velocity is very nearly constant throughout the vertical axis of the pipe, and gradients become progressively restricted to the near wall vicinity. This change in the flow structure is clearly related to the onset of Taylor-Proudman columns previously noted when commenting figure 6. The same changes in the flow behavior are also observed at  $Re_b = 133000$  (bottom panels). However, when comparing cases with the same vale of  $N$  (e.g. panels (b) and (f)), one can observe that the tendency for the flow to become symmetric about the vertical axis is faster at higher  $Re_b$ , whereas the Ekman layers are visually thinner at the higher  $Re_b$ .

It is important to recognise the substantial difference of the present flow arrangement with respect to the case of a spanwise rotating channel which was considered by Kristoffersen & Andersson (1993). In that case the Taylor-Proudman columns are aligned parallel to the channel walls, hence they do not give rise to Ekman layers, which in pipe flow are chiefly responsible for drag increase around the north and south poles, as figure 8 shows.

Figure 10 reports representative wall-normal axial velocity profiles in local wall units (i.e.

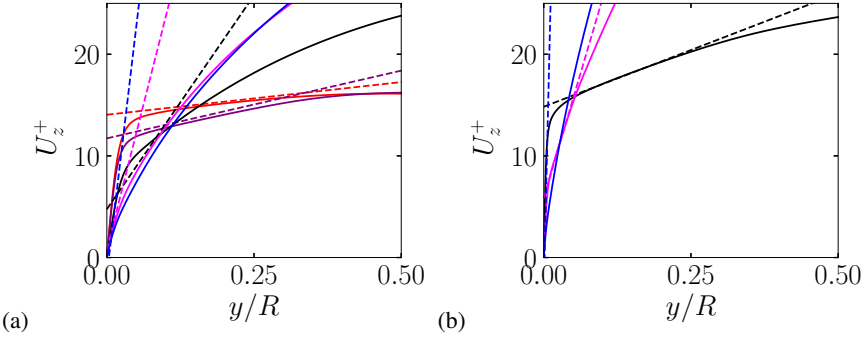


Figure 11: Inner-scaled wall-normal mean velocity profiles at  $\theta = 180^\circ$  (pressure side). Solid lines refer to DNS data and dashed lines to equation (3.1), for flow cases at  $Re_b = 17000$  (a) and cases at  $Re_b = 133000$  (b). Color codes are as in table 1.

263 based on the local friction velocity  $u_\tau = (\tau_w/\rho)^{1/2}$  as a function of the wall distance, to  
264 highlight deviations from the universal law-of-the-wall which is observed in non-rotating  
265 pipe flow. For the sake of clarity, the velocity profiles are shown up to the occurrence point  
266 of their first maximum. The figure shows that the velocity distributions on the suction side  
267 (orange shades) become immediately diverted from the logarithmic behavior, highlighting  
268 clear decrease of the local friction. The velocity profiles on the pressure side (in cyan shades)  
269 are more resilient to the effect of rotation, and a logarithmic layer is still observed at low  
270 rotation numbers. At intermediate rotation numbers, the logarithmic part of the velocity  
271 profiles is shifted downwards, indicating increase of the local friction, until the logarithmic  
272 layer becomes entirely disrupted at  $N \gtrsim 1$ . As seen in the bottom panels, increase of the  
273 Reynolds number mainly implies greater robustness of the logarithmic behavior, which  
274 persists until  $N \approx 1$  at  $Re_b = 133000$ .

275 Yang *et al.* (2020) argued that, for a channel that rotates about its spanwise axis at a  
276 reasonably high speed, the mean flow near the pressure side should follow a linear scaling,  
277 i.e.

$$278 \quad U_z^+ = 2 \frac{\Omega y}{u_\tau} + C, \quad (3.1)$$

279 with additive constant

$$280 \quad C = \frac{1}{\kappa} \log \left( \frac{u_\tau^2}{\nu \Omega} \right). \quad (3.2)$$

281 This prediction is compared with the DNS data in figure 11, where we have assumed  $\kappa = 0.33$ .  
282 We find that the scaling holds with reasonable accuracy for cases with intermediate rotation  
283 rate, specifically for  $N = 0.25, 0.5$  at  $Re_b = 17000$  and for  $N = 0.5, 2.0$  at  $Re_b = 133000$ ,  
284 but it clearly fails at high rotation rates as the flow relaminarises.

285 The statistics of the turbulence kinetic energy ( $k = \langle u_i u_i \rangle / 2$ ) are examined in figure 12. As  
286 for the mean velocity, we find that axial symmetry observed in non-rotating cases is broken in  
287 the presence of but weak rotation. At low rotation numbers (panel (a)) the magnitude of the  
288 buffer-layer peak along the horizontal symmetry axis of the pipe (orange shades) increases  
289 on the pressure side and decreases on the suction side, in response to increase and decrease  
290 of the imposed shear, respectively. Relaminarisation of the flow occurs on the suction side  
291 of the pipe already at  $N \approx 0.125$ . The buffer-layer peaks along the polar direction (purple  
292 shades) are instead barely affected. The most notable feature in the weak rotation regime is  
293 the reduction and flattening of  $k$  in the interior part of the pipe. This tendency becomes most  
294 evident as  $N$  increases, with suppression of the turbulence kinetic energy in the entire flow

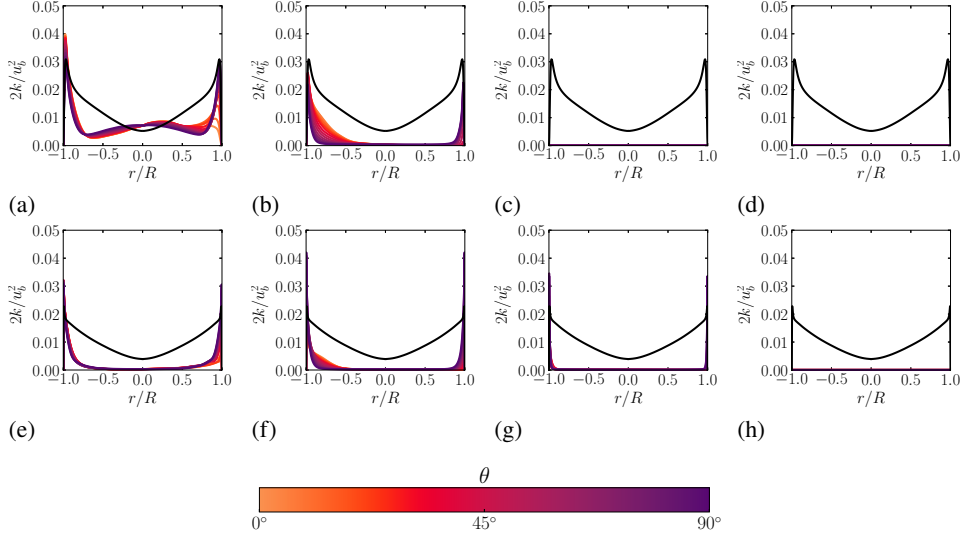


Figure 12: Radial profiles of outer-scaled turbulence kinetic energy at various azimuthal positions, for flow cases at  $Re_b = 17000$  (a-d), and  $Re_b = 133000$  (e-h). Only the interval  $\theta = [0^\circ, 90^\circ]$  is shown, at stations spaced  $7.5^\circ$  apart, with negative values of  $r$  signifying profiles taken at  $\theta + 180^\circ$ . (a)  $N = 0.03125$ , (b)  $N = 0.5$ , (c)  $N = 2.0$ , (d)  $N = 8.0$ . (e)  $N = 0.1$ , (f)  $N = 0.5$ , (g)  $N = 2.0$ , (h)  $N = 16.0$ . The black solid line denotes the mean turbulence kinetic energy profile in the non-rotating case.

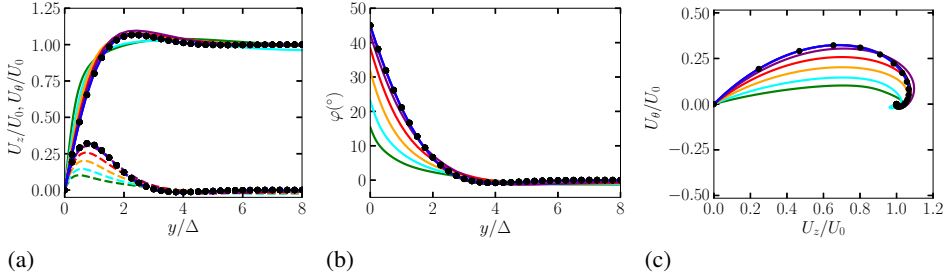


Figure 13: Profiles of mean axial ( $U_z$ ) and azimuthal ( $U_\theta$ ) velocity (a), wall-parallel flow angle  $\varphi = \tan^{-1}(U_\theta/U_z)$  (b) and hodograph diagram (c) at the polar coordinate  $\theta = \pi/2$  (north pole of the pipe). Data are shown for  $Re_b = 17000$ , at various rotation numbers:  $N = 0.03125$ ,  $N = 0.0625$ ,  $N = 0.125$ ,  $N = 0.25$ ,  $N = 0.5$ ,  $N = 2.0$ ,  $N = 4.0$ ,  $N = 8.0$ , see table 1 for the color codes. The velocity profiles are scaled by the mean centreline axial velocity  $U_0$ . The black circles denote the analytical solution for a laminar Ekman layer (Greenspan 1968).

295 field, at  $N \gtrsim 2$ . A similar scenario is also found at the higher  $Re_b$  (bottom row), at which  
296 however some signs of turbulence activity are still visible at the pressure side, even at  $N = 2$   
297 (panel (g)). The flow is found to be fully laminar at  $N = 16$ .

298 As noted when commenting figure 9, starting from rotation numbers of the order of unity,  
299 the flow exhibits the clear hallmark of Ekman layers, namely thin layers in which the direction  
300 of the wall-parallel velocity changes as a result of varying relative importance of imposed  
301 pressure gradient, Coriolis and viscous forces. The laminar Ekman solution for rotating flow

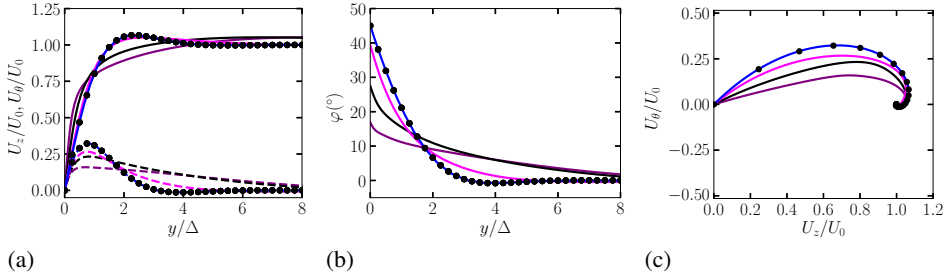


Figure 14: Profiles of mean axial ( $U_z$ ) and azimuthal ( $U_\theta$ ) velocity (a), wall-parallel flow angle  $\varphi = \tan^{-1}(U_\theta/U_z)$  (b) and hodograph diagram (c) at the polar coordinate  $\theta = \pi/2$  (north pole of the pipe). Data are shown for  $Re_b = 133000$ , at various rotation numbers:  $N = 0.1, N = 0.5, N = 2.0, N = 16.0$ , see table 1 for the color codes. The velocity profiles are scaled by the mean centreline axial velocity  $U_0$ . The black circles denote the analytical solution for a laminar Ekman layer (Greenspan 1968).

302 over a flat wall reads (Greenspan 1968)

$$303 \quad \frac{U_z(y)}{U_g} = 1 - e^{-y/\Delta} \cos\left(\frac{y}{\Delta}\right), \quad (3.3a)$$

304

$$305 \quad \frac{U_\theta(y)}{U_g} = e^{-y/\Delta} \sin\left(\frac{y}{\Delta}\right), \quad (3.3b)$$

306 where  $y$  is the wall distance,  $U_g$  is the intensity of the asymptotic (geostrophic) wind, and  
 307  $\Delta = (\nu/\Omega)^{1/2}$  is the thickness of the Ekman layer. The Ekman layer in the vicinity of the  
 308 north pole of the pipe (namely,  $\theta = 90^\circ$ ), is analysed in figure 13, where the wall distance is  
 309 scaled with respect to the Ekman length scale, and the geostrophic wind intensity is assumed  
 310 to be the mean velocity at the pipe centreline, say  $U_0$ . The individual axial and azimuthal  
 311 velocity components are shown in panel (a), the flow angle with respect to the axial direction  
 312 is shown in panel (b), and the projection in the hodograph plane is shown in panel (c).  
 313 As the rotation number increases the figure shows the onset of an overshoot of the axial  
 314 velocity, and the presence of a non-zero azimuthal velocity component. As a consequence,  
 315 the flow becomes diverted from the axial direction, to an extent which is proportional to  $N$ .  
 316 Excellent agreement between the computed profiles at high values of the rotation number  
 317 and the theoretical prediction given in equation (3.3) is found. This is in our opinion a rather  
 318 remarkable result, as the laminar Ekman solution is derived for the case of wall-normal  
 319 rotation over a flat wall. Here, we find that it also applies with excellent accuracy to flow  
 320 over a curved surface, with an effective rotation rate given by the wall-normal projection of  
 321 the angular velocity vector. The same considerations apply for the highest tested Reynolds  
 322 number (see figure 14), for which a laminar Ekman layer is found at  $N = 16$ .

#### 323 4. Friction

324 Frictional drag in pipes is obviously a parameter of paramount importance as it is related to  
 325 power expenditure to sustain the flow. Based on the flow analysis reported in the previous  
 326 section, herein we attempt to derive predictive formulas for the overall friction coefficient as a  
 327 function of the controlling parameters, namely Reynolds and rotation numbers. Preliminarily,  
 328 we note the presence of two limit cases, namely the rapid-rotation case ( $N \gg 1$ ) and the  
 329 non-rotating case ( $N = 0$ ). As for the case flow with no rotation, the Prandtl friction law for

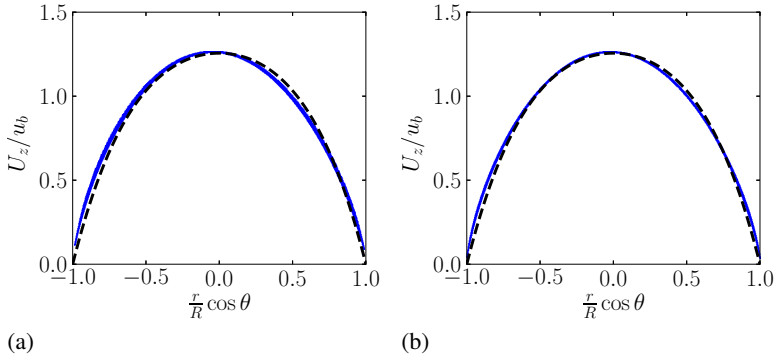


Figure 15: Scatter plots of mean axial velocity as a function of the horizontal coordinate, for  $Re_b = 17000$ ,  $N = 8$  (a) and  $Re_b = 133000$ ,  $N = 16$  (b), in blue. Only points at wall distance greater than five Ekman layer thicknesses are shown. The black dashed lines denote the velocity profile given in equation (4.2).

smooth pipes is known to perform very well, namely

$$1/\lambda_0^{1/2} = A \log 10 \left( Re_b \lambda_0^{1/2} \right) - B, \quad (4.1)$$

where  $\lambda_0$  is the friction factor for the non-rotating case at a given  $Re_b$ , and  $A \approx 2.102$ ,  $B \approx 1.148$ , as obtained from fitting DNS data (Pirozzoli *et al.* 2021).

In the opposite case of rapid rotation an approximate theoretical treatment is possible as the flow tends to become fully laminar. As a first step for that purpose, we recall that analysis of the mean velocity maps in figures 6 and 7 shows that, with exception of the near-wall Ekman layers, the mean axial velocity becomes solely a function of the horizontal direction as a result of the Taylor-Proudman theorem. Hence, in figure 15 we show a scatter plot of the mean axial velocity as a function of the horizontal coordinate ( $x_1 = r \cos \theta$ ), after removing points closer to the wall than  $5\Delta$ , which roughly corresponds to the effective thickness of the Ekman layer. The figure shows that, regardless of the Reynolds number, all data points fall on the same distribution, thus corroborating the initial assumption. Furthermore, we find that a convenient fit for the axial velocity distribution is as follows

$$\frac{U_{z,e}(r, \theta)}{u_b} = A \left[ 1 - \left( \frac{r}{R} \right)^2 \cos^2 \theta \right] + B \left[ 1 - \left( \frac{r}{R} \right)^2 \cos^2 \theta \right]^2, \quad (4.2)$$

with  $A = 1.74$ ,  $B = -0.484$  as determined from fitting the DNS data, which also lends itself to simple mathematical manipulations. Lack of perfect symmetry in figure 15 is rather apparent, which could be incorporated in equation (4.2), however the practical impact of such corrections on the overall friction would be minimal.

As for the mean axial velocity profiles within the Ekman layer, equation (3.3a) is adapted to the present case by assuming that: i) the local effective angular velocity at a given azimuthal angle is the wall-normal component, namely  $\Omega \sin \theta$ ; ii) the effective geostrophic velocity is the wall limiting value of the mean velocity distribution in the pipe core, as given in equation (4.2), hence we set  $U_g(\theta) = U_{z,e}(R, \theta)$ .

These assumptions are scrutinised in figure 16, where we show the mean axial velocity profiles as a function of the wall distance, scaled respectively by the assumed geostrophic velocity and by the local Ekman layer thickness. Several profiles are along the pipe perimeter are shown, with exception of those at  $\theta = 0^\circ$  and  $\theta = 180^\circ$ , where  $U_{z,e} = 0$ . The cases with highest rotation numbers for each extreme Reynolds number are reported in the figure. The

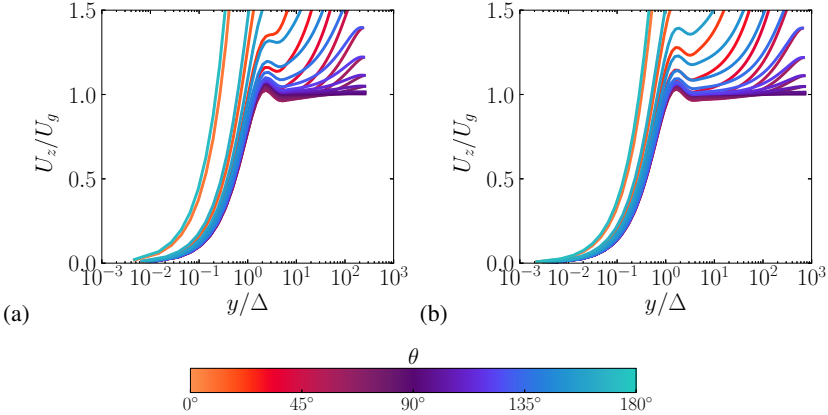


Figure 16: Mean axial velocity profiles scaled by the local geostrophic velocity ( $U_g$ ), as a function of wall distance normalised by the local Ekman layer thickness,  $\Delta = (\nu/(\Omega \sin \theta))^{1/2}$ , at  $Re_b = 17000$ ,  $N = 8$  (a), and  $Re_b = 133000$ ,  $N = 16$  (b). Profiles along the pipe perimeter are shown in intervals of  $7.5^\circ$ , with exception of  $\theta = 0^\circ$ ,  $\theta = 180^\circ$ .

figure confirms that the local Ekman layer thickness ( $\Delta = (\nu/(\Omega \sin \theta))^{1/2}$ ) is the correct length scale for the velocity profiles, as it yields universality of the velocity overshoot point, which occurs at  $y \approx 2.3\Delta$ , regardless of the azimuthal positions. Whereas the profiles near the north pole  $\theta = 90^\circ$ , exhibit perfect agreement with the canonical Ekman solution, good agreement is also observed at all azimuthal positions.

A prediction for the distribution of the wall friction along the pipe perimeter is then obtained from equation (3.3a), which upon differentiation at the wall yields

$$\frac{\tau_w}{\rho} = \nu \frac{dU_z}{dy} \Big|_{y=0} = \nu \frac{U_{z,e}(R, \theta)}{(\nu/(\Omega \sin \theta))^{1/2}}. \quad (4.3)$$

Using equation (4.2) to determine the geostrophic velocity one then obtains

$$\tau_w = 2^{1/2} \rho u_b^2 (\sin \theta)^{1/2} \left( \frac{N}{Re_b} \right)^{1/2} \left[ A \left( 1 - \cos^2 \theta \right) + B \left( 1 - \cos^2 \theta \right)^2 \right]. \quad (4.4)$$

This prediction is tested in figure 8 (dashed blue line in panels (a) and (c)), for the cases at the highest rotation number, for which it is found to yield an excellent approximation of the DNS data. Finally, the global friction factor is evaluated by averaging the wall shear stress (4.4) along the pipe perimeter, to obtain

$$\lambda = \frac{8\tau_w^*}{\rho u_b^2} = \frac{8}{\rho u_b^2} \frac{1}{2\pi} \int_0^{2\pi} \tau_w d\theta = k_E \left( \frac{N}{Re_b} \right)^{1/2}, \quad (4.5)$$

with  $k_E \approx 7.044$  resulting from integration.

This is the key prediction of the present study, which implies that the similarity parameter for friction in the rapidly rotating pipe regime is  $N/Re_b$ . This prediction is in line with the analysis of Pallares *et al.* (2005), who derived a similar scaling for the friction coefficient at the lateral walls of rotating square ducts. Figure 17(a) compares the prediction of equation (4.5) with the DNS data at various  $N, Re_b$ . The agreement is remarkably good provided  $(N/Re_b)^{1/2} \geq 0.005$ . Finally, to achieve continuous transition from the non-rotating

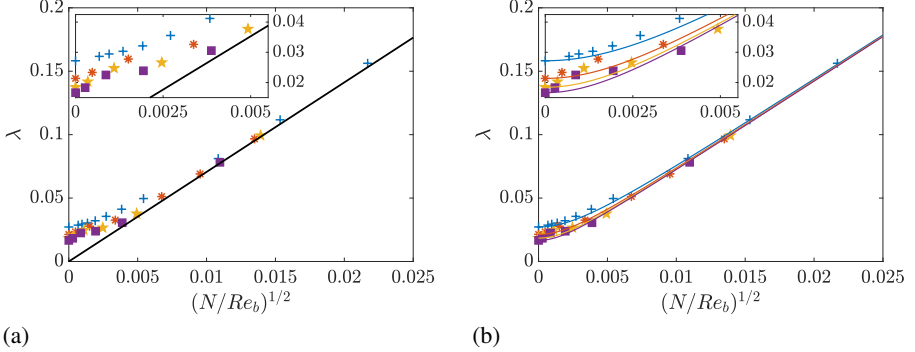


Figure 17: Distribution of friction factor as a function of  $(N/Re_b)^{1/2}$ , for DNS data at  $Re_b = 17000$  (+),  $Re_b = 44000$  (\*),  $Re_b = 82500$  (★),  $Re_b = 133000$  (■). In panel (a) the solid line denotes the asymptotic prediction for the rapid-rotation regime (4.5). Lines in (b) denote prediction of the interpolation formula (4.6) at  $Re_b = 17000$  (blue),  $Re_b = 44000$  (red),  $Re_b = 82500$  (orange),  $Re_b = 133000$  (purple).

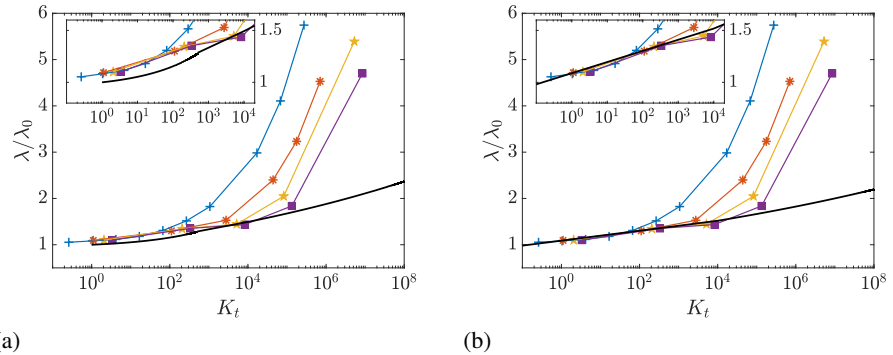


Figure 18: Distribution of friction factor (normalised by the non-rotating case value) as a function of the parameter  $K_t = Re_b N^2 / 4$  (Ito & Nanbu 1971), for DNS data at  $Re_b = 17000$  (+),  $Re_b = 44000$  (\*),  $Re_b = 82500$  (★),  $Re_b = 133000$  (■). In panel (a) the black line denotes the composite correlation (4.7)+(4.8), and in panel (b) the power-law fit (4.9).

381 case to the rapidly-rotating regime, we propose a simple interpolation of the form

$$382 \quad \lambda = \left( \lambda_0^2 + k_E^2 \frac{N}{Re_b} \right)^{1/2}, \quad (4.6)$$

383 with  $\lambda_0$  defined in equation (4.1). The results of the proposed interpolation formula are show  
384 in figure 17(b) which indicate reasonable prediction of the friction factor also in the regime  
385 of intermediate rotation. However, the DNS data seem to exhibit non-monotonic behavior at  
386  $N \approx 0.025$  (see the inset in panel (b)), which is not reproduced by equation (4.6).

387 For completeness, we also report a comparison of our DNS results with the correlation  
388 proposed by Ito & Nanbu (1971). According to their study, the similarity parameter for  
389 friction in the turbulent regime is  $K_t = Re_b N^2 / 4$ . Those authors found empirically that, for  
390  $1 \leq K_t \leq 500$ , the ratio of the friction coefficient with respect to the non-rotating case is

391 approximately

$$392 \quad \frac{\lambda}{\lambda_0} = 0.942 + 0.058K_t^{0.282}, \quad (4.7)$$

393 whereas at larger  $K_t$  one should use

$$394 \quad \frac{\lambda}{\lambda_0} = 0.924K_t^{0.05}. \quad (4.8)$$

395 In figure 18 we compare the above empirical formulas with the DNS data. Use of the parameter  
 396  $K_t$  indeed yields satisfactory universality of the friction data in the range of modest rotation  
 397 numbers, at which friction increase with respect to the non-rotating case is no more than  
 398 30%, however discrepancies at high rotation rates are very large. In this range of parameters  
 399 the correlation of Ito & Nanbu (1971) is consistent with the DNS data, but not quantitatively  
 400 accurate. We find that a better empirical fit is given by the power-law formula

$$401 \quad \frac{\lambda}{\lambda_0} = 1.05K_t^{0.04}. \quad (4.9)$$

402 As shown in panel (b), this formula is significantly more accurate at low values of  $K_t$ . Analysis  
 403 of the zoomed inset within Figure 17(b) reveals a non-trivial trend of the friction factor within  
 404 the Reynolds number range from 44000 to 133000. Notably, at the lowest rotation rates the  
 405 friction factor exhibits steeper growth than given in equation (4.6), which leads us to suggest  
 406 the correlation (4.9) in that regime.

## 407 5. Conclusions

408 Numerical investigation of flow in a rotating pipe through DNS has unveiled a rather complex  
 409 scenario, which includes disparate flow regimes, whose occurrence critically depends on the  
 410 delicate balance between rotational, inertial, and viscous forces. In particular, in contrast to the  
 411 case of flow in a non-rotating pipe, we have observed strong inhomogeneity of the flow along  
 412 the azimuthal direction, with local flow features being primarily controlled by the rotation  
 413 number. Specifically, at low rotation numbers, the flow features strong asymmetry between  
 414 the pressure side where turbulence intensifies and the local friction coefficient increases,  
 415 and the suction side, where turbulence is significantly suppressed, even under very modest  
 416 rotation rates. In this regime, the poles of the pipe aligned with the rotation axis, are relatively  
 417 unaffected. As a result, friction increases mildly as compared to the non-rotating case, at a  
 418 rate which is reasonably well predicted by the correlation (4.9), which is an improvement  
 419 over empirical formulas proposed in previous studies based on experimental campaigns (Ito  
 420 & Nanbu 1971). At higher rotation numbers, the effects of rotation manifest themselves more  
 421 clearly with the formation of Taylor-Proudman columns, with accumulation of momentum  
 422 in the central part of the pipe, and return to a symmetric state, whereby the pressure side of  
 423 the pipe also tends to attain a laminar state, along with the rest of the flow. In this regime the  
 424 flow features a core region with flow properties depending only on the direction normal to  
 425 the angular velocity, and thin laminar Ekman layers adjacent to the walls, across which the  
 426 magnitude and the flow direction change abruptly. **The most important observation based on**  
 427 **the DNS data is that the wall-normal velocity profiles within the Ekman layers at a given**  
 428 **azimuthal coordinate are very accurately parametrised in terms of the local wall-normal**  
 429 **projection of the angular velocity with associated viscous length scale, and of the local value**  
 430 **of the core velocity.** This finding allows a boundary-layer-like theory to be developed and  
 431 applied for the prediction of the local and global friction coefficients. The analysis highlights  
 432 the crucial importance of the parameter  $N/Re_b$  in controlling the fast-rotation regime of  
 433 motion. Indeed, in agreement with studies for square ducts (Pallares *et al.* 2005), we find

$Re_b$	$Re_\tau$	$N$	$L_z/R$	$N_z \times N_r \times N_\theta$	$\lambda \times 10^{-2}$	Line
17000	669	0.5	15	769 $\times$ 97 $\times$ 769	4.963	—
17000	669	0.5	30	1537 $\times$ 97 $\times$ 769	4.963	—
17000	669	0.5	45	2305 $\times$ 97 $\times$ 769	4.963	—
17000	670	0.5	15	769 $\times$ 193 $\times$ 769	4.977	—
17000	669	0.5	15	769 $\times$ 97 $\times$ 1537	4.966	—

Table 2: Computational parameters for grid sensitivity study. See table 1 for the nomenclature.

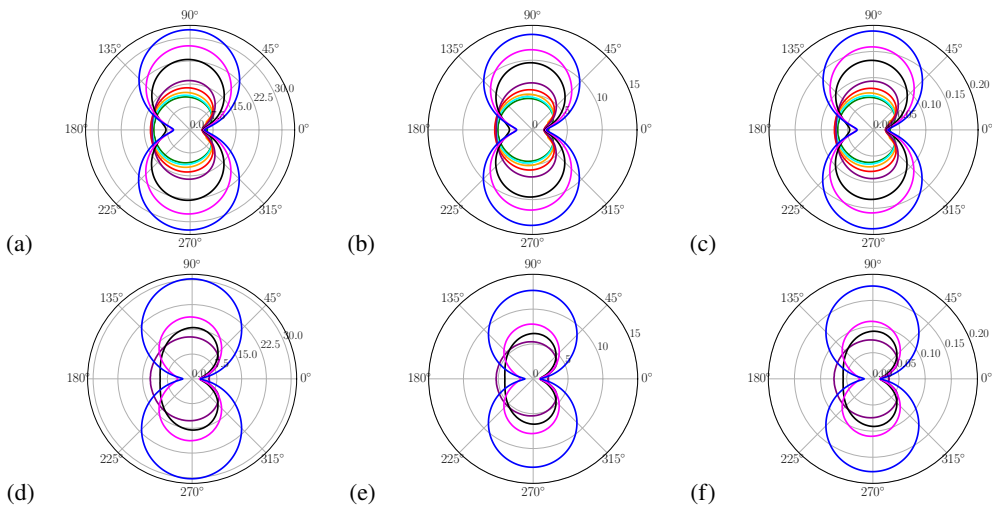


Figure 19: Polar distribution of the inner-scaled grid spacings, at  $Re_b = 17000$  (a, b, c), and  $Re_b = 133000$  (d, e, f): streamwise spacing  $\Delta z^+$  (a,d), azimuthal spacing  $R^+ \Delta\theta$  (b,e), and radial spacing at the wall  $\Delta r_w^+$  (c,f). The color codes correspond to different values of  $N$ , as given in table 1.

434 that  $\lambda \sim (N/Re_b)^{1/2}$ , hence the friction factor increases with the rotation number at much  
435 faster rate than in the low- $N$  regime. In the case of low-to-moderate rotation number the  
436 assumptions behind our theoretical analysis are not satisfied, hence empirical power-law  
437 correlations such as the one by Ito & Nanbu (1971), can provide more accurate predictions  
438 after suitable tuning of the coefficients. We expect that these insights into the effect of rotation  
439 on frictional drag can have significant implications for the design and operation of  
440 engineering applications where controlling or harnessing rotational effects is crucial.

## 441 Appendix A.

442 Given the complex nature of the flow under scrutiny we have carried out a comprehensive  
443 study of the effect of the pipe length and grid resolution on the flow statistics. General  
444 guidelines for the selection of the grid spacings in wall-bounded flows were provided by  
445 Hoyas & Jiménez (2006), namely that the streamwise spacing should be  $\Delta z^+ \lesssim 10$ , the  
446 spanwise spacing should be  $R^+ \Delta\theta \lesssim 5$ , and the wall-normal spacing at the wall should be  
447  $\Delta r_w^+ \ll 1$ . Figure 19 reports the azimuthal distribution of the grid spacings for all flow  
448 cases herein computed. In cases with low rotation rate and fully turbulent flow, the previous

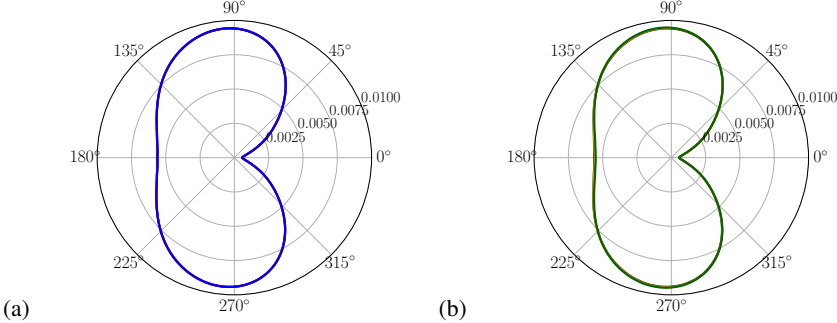


Figure 20: Polar distribution of the local streamwise wall shear stress ( $\tau_w$ ), normalised by the reference dynamic pressure  $\rho u_b^2$  at  $Re_b = 17000$ , and  $N = 0.5$ . (a) effects of domain length, (b) effects of grid refinement. The color codes correspond to the different runs of the grid sensitivity study, as given in table 2.

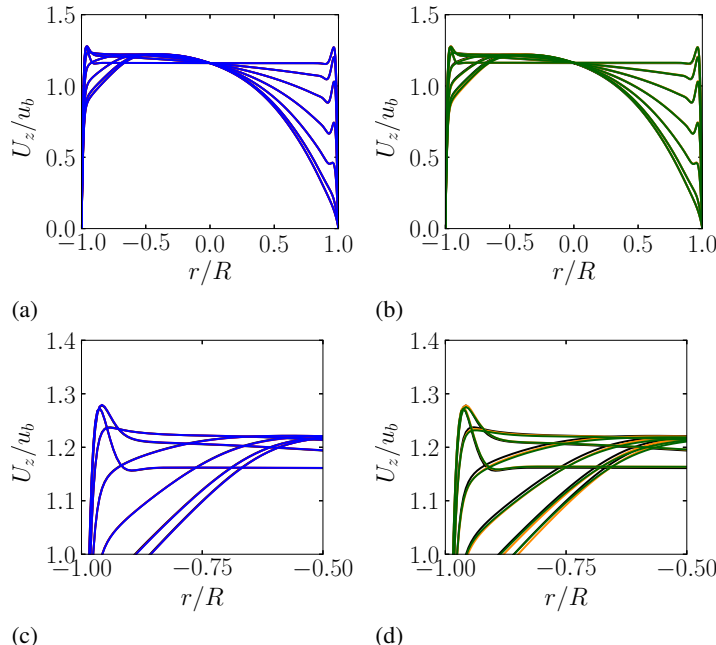


Figure 21: Radial profiles of outer-scaled axial velocity at various azimuthal positions, for flow cases at  $Re_b = 17000$ , and  $N = 0.5$ . Only the interval  $\theta = [0^\circ, 90^\circ]$  is shown, at stations spaced  $15^\circ$  apart, with negative values of  $r$  signifying profiles taken at  $\theta + 180^\circ$ . (a,c) effects of pipe length, (b,d) effects of grid refinement. The color codes correspond to the different runs of the grid sensitivity study, as given in table 2.

449 prescriptions are in fact satisfied. However, these putative upper bounds are exceeded in flows  
 450 with high rotation rate. This observation could convey the false impression that the DNS are  
 451 under-resolved, whereas it is rather associated with the occurrence of a locally laminar flow  
 452 state, to which the traditional estimates do not apply. For complex flows as the one under  
 453 scrutiny here only a grid resolution study, which we report hereafter, can provide guidance  
 454 for the selection of grid and computational box size. For that purpose, a representative flow  
 455 case with moderate rotation rate has been considered, namely  $Re_b = 17000$ ,  $N = 0.5$ .  
 456 A summary of the relevant simulations we have carried out is given in table 2, whereby

457 we have doubled or tripled the pipe length, and doubled the number of grid points along  
 458 the azimuthal and radial directions. As a first confirmation that grid convergence of the  
 459 statistics is achieved, the table shows differences of no more than 0.3% in the global friction  
 460 coefficient, as compared to the baseline simulation. This conclusion is corroborated from  
 461 figure 20, showing the azimuthal distribution of the local streamwise wall shear stress. Again,  
 462 the influence of pipe length (a) and grid resolution (b) is seen to be negligible, showing overall  
 463 relative differences smaller than 0.6% for cases with finer grids. Last, in figure 21 we show  
 464 the outer-scaled velocity profiles in the wall-normal direction. The profiles are found to be  
 465 identical on the suction side and only exhibit small differences (of less than 0.7%) on pressure  
 466 side for cases with finer grids.

467 **Acknowledgements.** We acknowledge the CINECA award under the ISCRA initiative, for the availability of  
 468 high-performance computing resources and support. The authors thank Yu Ming for the insightful exchange  
 469 of ideas regarding the topic of the manuscript.

470 **Funding.** This research received funds from ICSC – Italian Research Center on High Performance  
 471 Computing, Big Data and Quantum Computing - Spoke 6, funded by European Union – NextGenerationEU  
 472 (CUP B83C22002830001).

473 **Declaration of interests.** The authors report no conflict of interest.

474 **Data availability statement.** The data that support the findings of this study are openly available at the web  
 475 page <http://newton.dma.uniroma1.it/database>.

476 **Author ORCID.** A. Ceci <https://orcid.org/0000-0001-6664-1677>  
 S. Pirozzoli <https://orcid.org/0000-0002-7160-3023>

## REFERENCES

- 477 AKSELVOLL, K. & MOIN, P. 1996 An efficient method for temporal integration of the Navier-Stokes equations  
 478 in confined axisymmetric geometries. *J. Comput. Phys.* **125**.
- 479 ATKINS, NICHOLAS R & KANJIRAKKAD, VASUDEVAN 2014 Flow in a rotating cavity with axial throughflow  
 480 at engine representative conditions. In *Turbo Expo: Power for Land, Sea, and Air*, , vol. 45738, p.  
 481 V05CT16A041. American Society of Mechanical Engineers.
- 482 BARUA, S.N. 1954 Secondary flow in a rotating straight pipe. *Proc. R. Soc. London. Series A* **227**, 133–139.
- 483 BENTON, G.S. & BOYER, D. 1966 Flow through a rapidly rotating conduit of arbitrary cross-section.  
*J. Fluid Mech.* **26**, 69–79.
- 485 COLETTI, FILIPPO, JACONO, DAVID LO, CRESCI, IRENE & ARTS, TONY 2014 Turbulent flow in rib-roughened  
 486 channel under the effect of coriolis and rotational buoyancy forces. *Physics of fluids* **26** (4).
- 487 COLETTI, FILIPPO, MAURER, THOMAS, ARTS, TONY & DI SANTE, ALBERTO 2012 Flow field investigation in  
 488 rotating rib-roughened channel by means of particle image velocimetry. *Experiments in fluids* **52**,  
 489 1043–1061.
- 490 DAI, Y.-J., HUANG, W.-X., XU, C.-X. & CUI, G.-X. 2015 Direct numerical simulation of turbulent flow in a  
 491 rotating square duct. *Phys. Fluids* **27**.
- 492 FANG, X., YANG, Z., WANG, B.-C. & BERGSTROM, D. J. 2017 Direct numerical simulation of turbulent flow  
 493 in a spanwise rotating square duct at high rotation numbers. *Int. J. Heat Fluid Flow* **63**, 88–98.
- 494 FATICA, M. & RUETSCH, G. 2014 *CUDA Fortran for scientists and engineers*. Elsevier.
- 495 GREENSPAN, H.P. 1968 *The theory of rotating fluids*. Cambridge University Press Cambridge.
- 496 GREITZER, E. M., TAN, C. S. & GRAF, M. B. 2007 *Internal flow: concepts and applications*. Cambridge  
 497 University Press.
- 498 HOYAS, S. & JIMÉNEZ, J. 2006 Scaling of velocity fluctuations in turbulent channels up to  $Re_\tau = 2003$ .  
*Phys. Fluids* **18**, 011702.
- 500 ISHIGAKI, H. 1996 Analogy between turbulent flows in curved pipes and orthogonally rotating pipes.  
*J. Fluid Mech.* **307**, 1–10.
- 502 ITO, H. & NANBU, K. 1971 Flow in Rotating Straight Pipes of Circular Cross Section. *J. Basic Eng.* **93**,  
 503 383–394.
- 504 JACKSON, RICHARD W, LUBERTI, DARIO, TANG, HUI, POUNTNEY, OLIVER J, SCOBIE, JAMES A, SANGAN,  
 505 CARL M, OWEN, J MICHAEL & LOCK, GARY D 2021 Measurement and analysis of buoyancy-induced

- 506 heat transfer in aero-engine compressor rotors. *Journal of Engineering for Gas Turbines and Power*  
 507 **143** (6), 061004.
- 508 JOHNSTON, J. P., HALLENT, R. M. & LEZIUS, D. K. 1972 Effects of spanwise rotation on the structure of  
 509 two-dimensional fully developed turbulent channel flow. *J. Fluid Mech.* **56**, 533–557.
- 510 KIM, J. & MOIN, P. 1985 Application of a fractional-step method to incompressible navier-stokes equations.  
 511 *J. Comput. Phys.* **59**, 308–323.
- 512 KRISTOFFERSEN, R. & ANDERSSON, H. I. 1993 Direct simulations of low-reynolds-number turbulent flow in  
 513 a rotating channel. *J. Fluid Mech.* **256**, 163–197.
- 514 LIGRANI, P. 2013 Heat transfer augmentation technologies for internal cooling of turbine components of gas  
 515 turbine engines. *Int. J. Rot. Machin.* **2013**.
- 516 LIOU, TM, CHANG, SW, HUNG, JH & CHIOW, SF 2007 High rotation number heat transfer of a 45 rib-  
 517 roughened rectangular duct with two channel orientations. *International Journal of Heat and Mass Transfer* **50** (19–20), 4063–4078.
- 518 LUBERTI, DARIO, PATINIOS, MARIOS, JACKSON, RICHARD W, TANG, HUI, POUNTNEY, OLIVER J, SCOBIE,  
 519 JAMES A, SANGAN, CARL M, OWEN, J MICHAEL & LOCK, GARY D 2021 Design and testing of a rig to  
 520 investigate buoyancy-induced heat transfer in aero-engine compressor rotors. *Journal of Engineering  
 521 for Gas Turbines and Power* **143** (4), 041030.
- 522 MÅRTENSSON, G., GUNNARSSON, J., JOHANSSON, A.V. & MOBERG, H. 2002 Experimental investigation of a  
 523 rapidly rotating turbulent duct flow. *Exp. Fluids* **33**, 482–487.
- 524 MORRIS, WD 1996 A rotating facility to study heat transfer in the cooling passages of turbine rotor blades.  
 525 *Proceedings of the Institution of Mechanical Engineers, Part A: Journal of Power and Energy* **210** (1),  
 526 55–63.
- 527 ORLANDI, P. 2000 *Fluid flow phenomena: a numerical toolkit*. Kluwer.
- 528 PALLARES, J. & DAVIDSON, L. 2000 Large-eddy simulations of turbulent flow in a rotating square duct. *Phys.  
 529 Fluids* **12**, 2878–2894.
- 530 PALLARES, J., GRAU, F. X. & DAVIDSON, L. 2005 Pressure drop and heat transfer rates in forced convection  
 531 rotating square duct flows at high rotation rates. *Phys. Fluids* **17**, 075102.
- 532 PIROZZOLI, S. & ORLANDI, P. 2021 Natural grid stretching for dns of wall-bounded flows. *J. Comput. Phys.*  
 533 **439**, 110408.
- 534 PIROZZOLI, S., ROMERO, J., FATICA, M., VERZICCO, R. & ORLANDI, P. 2021 One-point statistics for turbulent  
 535 pipe flow up to  $Re_\tau \approx 6000$ . *J. Fluid Mech.* **926**, A28.
- 536 PROUDMAN, J. 1916 On the motion of solids in a liquid possessing vorticity. *Proc. R. Soc. London. Series A*  
 537 **92** (642), 408–424.
- 538 ROSAS, R. H., ZHANG, Z.-P. & WANG, B.-C. 2021 Direct numerical simulation of turbulent elliptical pipe  
 539 flow under system rotation about the major axis. *Phys. Rev. Fluids* **6** (8), 084609.
- 540 SUN, ZIXIANG, GAO, FENG, CHEW, JOHN W & AMIRANTE, DARIO 2022 Large eddy simulation investigation  
 541 of low rossby number buoyant flow in rotating cavities. *Journal of engineering for gas turbines and  
 542 power* **144** (12), 121023.
- 543 TAYLOR, G.I. 1917 Motion of solids in fluids when the flow is not irrotational. *Proc. R. Soc. London. Series A*  
 544 **93** (648), 99–113.
- 545 VERZICCO, R. & ORLANDI, P. 1996 A finite-difference scheme for three-dimensional incompressible flows  
 546 in cylindrical coordinates. *J. Comput. Phys.* **123**, 402–414.
- 547 VISSCHER, JAN, ANDERSSON, HELGE I, BARRI, MUSTAFA, DIDELLE, HENRI, VIBOUD, SAMUEL, SOUS, DAMIEN  
 548 & SOMMERIA, JOËL 2011 A new set-up for piv measurements in rotating turbulent duct flows. *Flow  
 549 measurement and instrumentation* **22** (1), 71–80.
- 550 WU, X. & MOIN, P. 2008 A direct numerical simulation study on the mean velocity characteristics in  
 551 turbulent pipe flow. *J. Fluid Mech.* **608**, 81 – 112.
- 552 YANG, X. I. A., XIA, Z.-H., LEE, J., LV, Y. & YUAN, J. 2020 Mean flow scaling in a spanwise rotating channel.  
 553 *Phys. Rev. Fluids* **5**, 074603.
- 554 ZHANG, Z.-P. & WANG, B.-C. 2019 Direct numerical simulation of turbulent flow in a circular pipe subjected  
 555 to radial system rotation. *Flow Turbul. Combust.* **103**, 1057–1079.